Supplementary Material for:

Reaction mechanism of the ϵ subunit of *E. coli* DNA polymerase III: Insights into active site metal coordination and catalytically significant residues

G. Andrés Cisneros[a,*], Lalith Perera[a,*], Roel M. Schaaper[b], Lars C. Pedersen[a], Robert E. London[a], Lee G. Pedersen[a,c] and Thomas A. Darden[a]

[a] *Laboratory of Structural Biology, National Institute of Environmental Health Sciences, Research Triangle Park (RTP), NC, 27709.*

[b] *Laboratory of Molecular Genetics, National Institute of Environmental Health Sciences, Research Triangle Park (RTP), NC, 27709.*

[c] *Department of Chemistry, University of North Carolina Chapel Hill, NC 27599.*

I. DETAILED METHODS

In this section we present the computational details for the calculations. In subsection I A we provide the details of the methods used to obtain all three initial structures. This is followed by the details of the QM/MM optimization procedures in subsection I B. Finally, in subsection I C we describe the computational procedures employed to determine the reaction paths associated with the reaction mechanisms as well as the details for the residue analysis calculations.

A. Initial structure determination

All calculations were carried out with the AMBER suite of programs for structure setup and equilibration [1], and with modified versions of Gaussian (Ref. [40] from main text) and TINKER for the QM/MM reaction path calculations [2, 3]. The QM/MM optimizations were performed with an iterative method as described in [4, 5] using the pseudobond model for all boundary atoms [6, 7].

The X–ray structures for the ϵ186–HOT complex has recently been reported [8]. The pre–catalytic structure (pdb id 2IDO) consists of ϵ186, HOT and TMP. In this case, both dNTP–binding and catalytic metals have been assigned as Mn^{2+}. We have chosen this structure in order to have a good starting point for the reactant state in our calculations and to study the role of HOT in catalysis.

Initially, the structure was modified by replacing the Mn^{2+} by Mg^{2+} and TMP by a single stranded–DNA (ss–DNA) trinucleotide (dA–dC–dT) which was docked in the active site. Hydrogens were added to heavy atoms using XLeap [1]. This structures was solvated in TIP3P [9] water box and three counterions were included to neutralize the charge of the system. The system was relaxed by a series of molecular dynamics (MD) simulations using PMEMD and the AMBER99 force field [1]. The simulations were run for a total of 2 ns under periodic boundary conditions (PBC) with particle mesh Ewald (PME) for long–range electrostatics [10–12].

Following equilibration, the size of the system was decreased by reducing the solvent box. The final QM/MM system includes all atoms in the protein and a solvent sphere of 30 Å radius around the catalytic metal for a total of 18158 atoms for the ϵ186–HOT systems. The reason for this reduction is that our current QM/MM implementation does not include capabilities for PBC calculations.

B. QM/MM optimizations

Following equilibration the QM subsystem was chosen to include both active site metals, side chains of D12, E14, H162, D167, the dC nucleotide (excluding C5′ and the phosphate group), part of the dT nucleotide (phosphate bond and C5′) and five water molecules that complete the coordination spheres of the metals, for a total of 82 QM atoms including 6 boundary atoms (Cα of amino acids, C5′ of dC and C4′ of dT). All boundary atoms were treated with the pseudobond method [6, 7]. The remaining atoms were included in the MM subsystem and treated with the parm99 force field. Once the ϵ186–HOT(Mg^{2+}) structure was optimized, HOT was replaced by solvent and re–equilibrated to obtain the free–ϵ system (see main text), reducing the system size to 18043 total atoms (same number of atoms in the QM subsystem). This structure was used instead of starting from the reported free–ϵ X–ray crystal structure [13] in order to have similar references. In addition, both the free–ϵ and ϵ–HOT X–ray structures have been shown to be very similar, RMSD of 0.4 Å [8]. The product structures required for the path calculations were created from the reactant by manually modifying the coordinates with a graphical program. All structures were optimized iteratively [4].

QM subsystem optimizations were converged to the default values in Gaussian03. MM subsystem optimizations were converged to a gradient RMS 0.2 kcal/mol Å. In the case of the MM subsystem an active sphere of 20 Å around the active site was used, with a 15 Å cutoff for non–bonded interactions.

Geometry optimizations were carried out in an iterative fashion as mentioned above. In the case of the QM subsystem, all calculations were done at the B3LYP level [14, 15] with a mixed basis set where the 6–31G* basis was used for all reactive atoms: OD1 from E14, Nϵ from H162, O in one of the waters coordinating the nucleotide binding metal, O in the nucleophilic water and both Mg^{2+}. For the O3', O5' and P atoms (involved in the phosphate bond breaking and forming) the 6–31+G* basis was used . All other (non–reactive) QM atoms were represented with 3–21G. For Mn^{2+} the LANL2DZ pseudopotential was employed.

In the case of manganese as the catalytic metal, the issue of spin state arises. In this case there are several options due to the dual metal active site, including low spin (LS), high spin (HS) and broken–symmetry low spin (BSLS) states. Cluster calculations derived from the X–ray structure of DNA polymerase β [16] have showed that the energy difference between the HS and BSLS is relatively low, between 0.2 to 0.6 kcal/mol, whereas the difference between LS and HS is over 120 kcal/mol. In addition, approximating a BSLS state by a high spin state has been previously employed in DFT [17, 18]. Based on these results, all manganese calculations were done with the HS state (spin multiplicity of 11). More importantly, the 0.6 kcal/mol difference between the BSLS and the HS state is well below the accuracy of our method.

As explained above, all calculations involving Mn were performed using the LANL2DZ pseudopotential [19]. These pseudopotentials have been shown to give good geometries for Mn clusters and complexes themselves, as well as in combination with 6–31G* basis [20–23].

C. Reaction path and residue analysis calculations

The optimized end points for all three systems were used for the calculation of the initial reaction paths using a modified version of the quadratic string method (QSM) [24]. QSM is one of the so called "chain–of–replicas" methods where the reaction path is represented by a discrete number of structures that are optimized to the steepest descent path in parallel. There are several chain–of replicas methods including the Nudged Elastic Band [25, 26] and the Ayala and Schlegel algorithm [27]. We have previously extended both of these methods for the determination of enzymatic reaction paths [28–30]. QSM has been recently developed based on a multiobjective optimization framework. In this method, each replica along the path is minimized by integration in the descent direction. Each local integration is done on a quadratic surface approximated by a damped Broyden–Fletcher–Goldfarb–Shanno [31] Hessian.

Another difference between NEB and QSM is the way in which the images are spaced along the path. In NEB, the images are optimized with the constraint that the distance between points remains equal. QSM however, uses an iterative approach where the images are redistributed when needed along an interpolating polynomial. In this work we have modified QSM so that the cartesian degrees of freedom are separated into a "reactive set" and a "spectator" set and only the reactive set is used for the calculation of the distances in the redistribution step [30, 32]. In particular for this case, only the coordinates for the reactive atoms and both metals were included in the reactive set.

The initial QSM paths were optimized by including 8 replicas between the end–points to give a total of 10 initial points. These points were optimized iteratively in parallel using the same method as the QM/MM optimization. The initial guess to the path was obtained from a linear interpolation between the points for both QM and MM subsystems [24, 28]. During the path optimization, a constrained MM optimization was carried out to avoid path discontinuities [29, 30]. In this method, the MM subsystem is subjected to position constraints during the optimization and these constraints are reduced with each iteration [33]. The paths were considered optimized when the MM environment does not change from one path optimization cycle to the next.

Once the QSM paths were optimized, the highest points were optimized to the nearest transition state (TS) with the quadratic synchronous transit 3 (QST3) method [34, 35]. Following the TS optimizations, the legs of the path between the critical points were re–calculated with a larger number of points for a better description of the path. Initially QSM was attempted to calculate these paths, however, the only legs that were optimized without significant discontinuities were the ones corresponding to the free–ϵ186 path with Mg^{2+} . All other intermediate points were obtained with the coordinate driving method [36], with a step size of 0.1 Å. In the case of the paths for the protonation of O3', the same procedure was employed throughout and the intermediate points after TS optimization were obtained with QSM. The RCD method for enzyme calculations has been described in detail in [37].

The role of individual residues to the catalytic mechanism has been investigated by analyzing the non–bonded interactions of each residue with the QM subsystem [38]. Note that the information gained from this energy analysis is only qualitative. This analysis is achieved by calculating the changes in electrostatic and Van der Waals interaction energies between individual residues and the QM subsystem when the system goes from reactant to TS. The formula is $\Delta E_i = < E_{i/QM} >_{MM,TS} - < E_{i/QM} >_{MM,reactant}$, where <> denotes an ensemble average, i denotes an individual

residue (or water molecule) and $E_{i/QM}$ represents the electrostatic or Van der Waals interaction energies between the ith residue and the QM subsystem. ΔE_i can only be viewed as a first–order approximation to the stabilization of the TS since conformational changes and dielectric screening are not taken into account. Negative ΔE_i indicate a stabilization of the TS by that residue and a positive value indicates a destabilizing contribution. Finally, it should be noted that if a residue does not (de)stabilize the TS in this scheme it does not imply that this residue is not important to catalysis, since there can be other contributions such as binding the substrate or stabilizing the local or global structure for enzymatic activity. In all cases, the MM environment of the reactant and TS structures (QM subsystems fixed) [5] were equilibrated with AMBER for 300 ps and another 300 ps of production run were used to obtain 300 snapshots. These 300 snapshots per critical point were used for the calculation of the residue interaction in each case.

II. METAL COORDINATION DISTANCES

Table S1: Coordination distances (in Å) for the catalytic and nucleotide binding metals . [a]OP refers to the Oxygen atom from the phosphate group that bridges both metals. [b] O3'–P refers to the O3' on dC.

	ϵ–HOT(Mg^{2+})			ϵ–HOT(Mn^{2+})			free–ϵ(Mg^{2+})		
	Reactant	TS	Product	Reactant	TS	Product	Reactant	TS	Product
	Catalytic Metal								
OD1–D12	2.0	2.0	1.9	2.2	2.1	2.0	2.0	2.0	1.9
OD1–E14	1.9	1.9	2.0	2.0	2.0	2.1	1.9	1.9	2.0
OD2–D167	1.9	1.9	1.9	2.0	2.0	2.0	1.9	1.9	1.9
OP[a]	2.1	2.0	2.1	2.1	2.1	2.1	2.1	2.0	2.1
O–H_2O (nucl)	2.1	2.3	2.2	2.2	2.2	2.4	2.1	2.2	2.2
	Nucleotide Binding Metal								
OD2–D12	1.9	2.0	2.1	2.0	2.0	2.2	1.9	2.0	2.0
OP[a]	2.0	2.1	2.3	2.2	2.1	2.3	2.1	2.0	2.3
O3'–P[b]	2.2	2.1	2.0	2.3	2.2	2.0	2.2	2.1	1.9
O–H_2O	2.0	2.0	2.0	2.1	2.1	2.1	2.0	2.0	2.0
O–H_2O	2.0	2.0	2.0	2.1	2.1	2.1	2.0	2.0	2.0
O–H_2O	2.3	2.6	2.6	2.5	2.7	2.6	2.3	2.6	3.1

III. SUPERPOSITION OF ACTIVE SITES FOR ϵ186–HOT AND FREE–ϵ

Figure S1 shows the superposition of the active sites for the reactants, TS and products for ϵ186–HOT(Mg^{2+}) and free–ϵ186(Mg^{2+}).

Figure S1: Superposition of active sites for the calculated reactants (left), transition states (middle) and products (right). The ϵ186–HOT(Mg^{2+}) structure is shown in aquamarine with nucleophilic water in yellow and free–ϵ186(Mg^{2+}) is shown in orange with nucleophilic water in green. Electrophilic phosphate and waters coordinating the nucleotide binding metal are shown as spheres. Hydrogen atoms have been omitted for clarity.

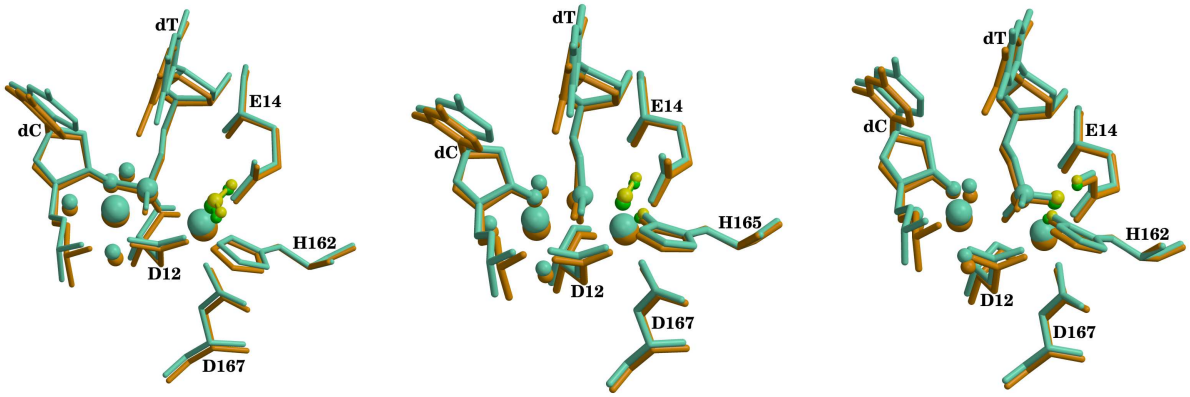

IV. QSM PATHS FOR PROTONATION OF O3'

As explained in the main text, the protonation of O3' on dC and deprotonation of H162 results in a lowering of the product structure with respect to the initial reactant. Two schemes were studied to test possible paths to transfer this proton. Both schemes involve the transfer of the proton through an oxygen on the phosphate of the excised dT nucleotide, either going "over" (on the nucleotide side) or "under" (on the metals side) the O atom. Figure S2 shows the two optimized TSs for the two deprotonation schemes for ϵ186–HOT and free–ϵ186 and Figure S3 shows the optimized product for ϵ186–HOT. The calculated QSM paths for both systems are shown in Figs. S4 and S5. As can be seen in both cases (ϵ186–HOT and free–ϵ186) the calculated barriers are above 30 kcal/mol for either the "over" or "under" schemes. In both cases the tested paths for the protonation of O3' involves the transfer of the proton on H162 (originally from the nucleophilic water) to an O atom on the phosphate of the excised nucleotide (dT). Subsequently the proton rotates about this O atom and transfers to the O3' (see Figs S2 and S3).

Figure S2: Active site for the calculated TSs for the protonation of O3' , left: "under", right: "over". The ϵ186–HOT structure is shown in aquamarine with nucleophilic water in yellow and free–ϵ186 is shown in orange with nucleophilic water in green. Electrophilic phosphate and waters coordinating the nucleotide binding metal are shown as spheres. Hydrogen atoms have been omitted for clarity.

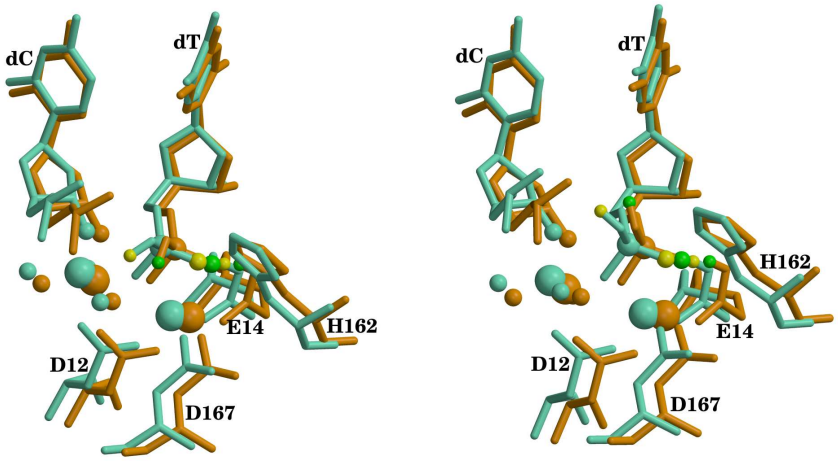

Figure S3: Active site for the calculated product for the protonation of O3' (ϵ186–HOT structure only).

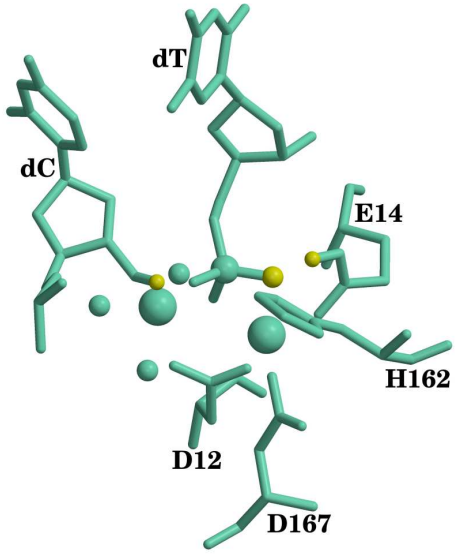

Figure S4: Calculated paths for the ϵ186–HOT proton transfer from H162 to O3' on dC. Left: "under", right: "over"

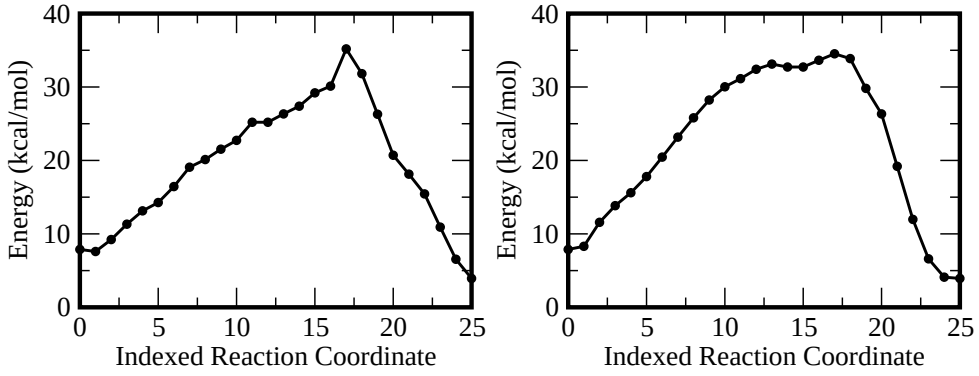

Figure S5: Calculated paths for the ϵ186–HOT proton transfer from H162 to O3' on dC. Left: "under", right: "over"

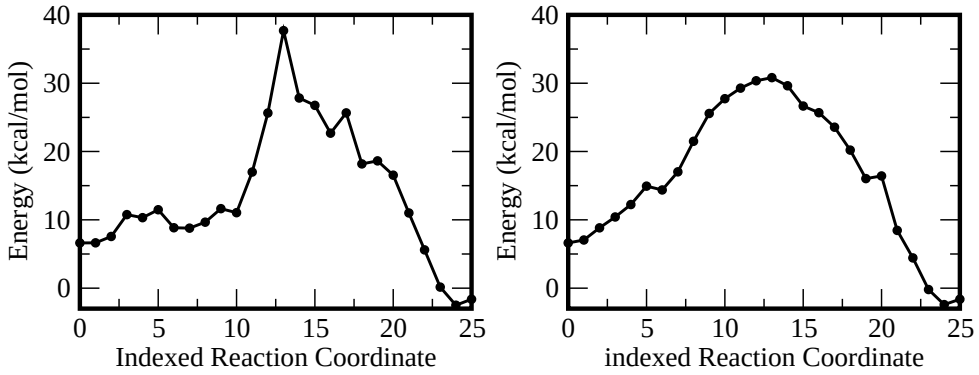

V. RESIDUE ANALYSIS

All residue analysis results include protein residues, nucleic acids and all solvating water molecules. As can be seen from Figures S6 and S7 there are only a few residues that have a significant contribution to the reactions ($|\Delta E_i| \geq 1$ kcal/mol). Residue numbers in Figures S6 and S7 are consecutive, 1 to 181 correspond to ϵ, 182–251 to HOT (in the complex cases), and the rest are water molecules and metals (including counterions).

Figure S6: Coulomb interaction per residue for all three systems (ϵ186 subunit only). Top: ϵ186–HOT(Mg^{2+}), middle: ϵ186–HOT(Mn^{2+}), bottom: free–ϵ186(Mg^{2+}).

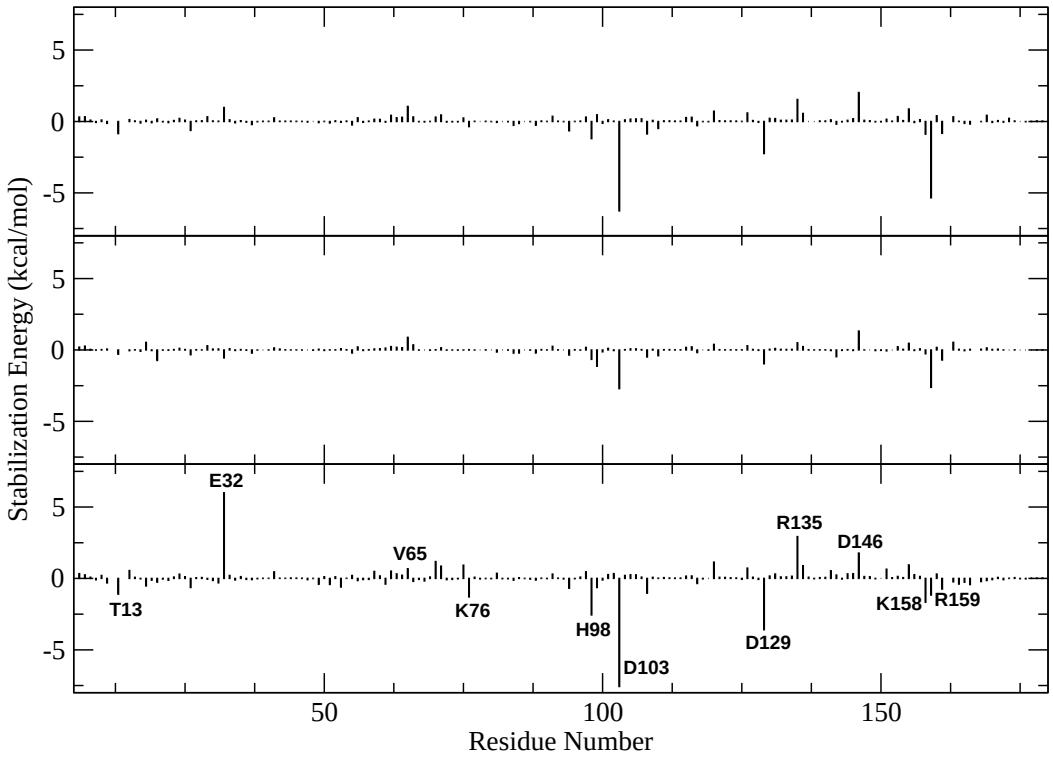

Figure S7: Coulomb interaction per residue for the ϵ186–HOT systems for HOT and counterions only. Top: Mg^{2+}, bottom: Mn^{2+}.

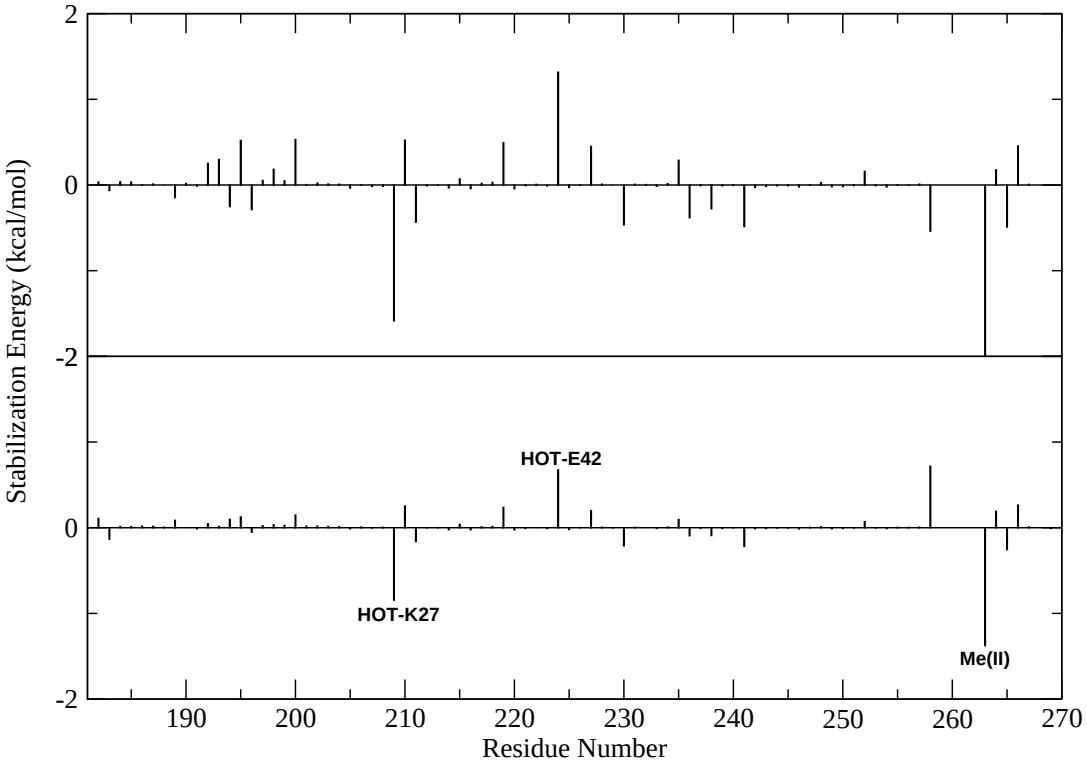

VI. STRUCTURAL ALIGNMENT

Figures S8 and S9 show the alignment of ϵ with the exonuclease domain (Klenow fragment) of DNA polymerase I from *E. coli* [39] and the exonuclease domain of the DNA polymerase from bacteriophage RB69 [40] respectively. As can be seen, the position of the conserved residues is similar to TREX1, which has been linked to several autoimmune diseases [41–43] (see main text).

Figure S8: Structural alignment comparing residues obtained from the decomposition analysis in ϵ186–HOT (light blue) superposed with the Klenow fragment (red). Residues from energy decomposition for ϵ186 are shown in green; structurally homologous residues for Klenow are shown in yellow. Metal binding residues (and H162) for ϵ186 are shown in light blue; structurally homologous active site residues for Klenow are shown in red.

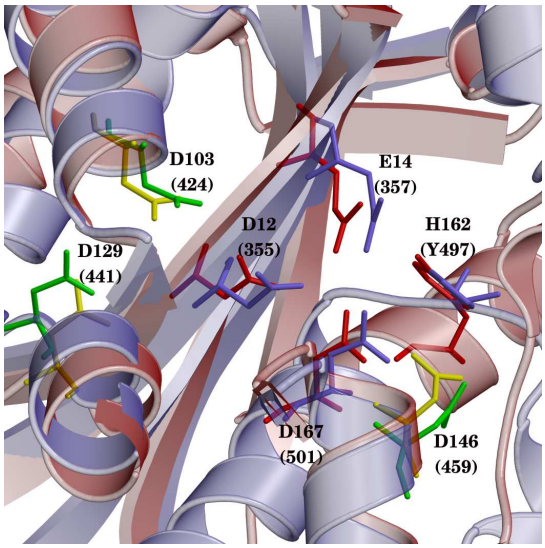

Figure S9: Structural alignment comparing residues obtained from the decomposition analysis in ϵ186–HOT (light blue) superposed with RB69 (red). Residues from energy decomposition for ϵ186 are shown in green; structurally homologous residues for RB69 are shown in yellow. Metal binding residues for ϵ186 are shown in light blue; structurally homologous active site residues for RB69 are shown in red.

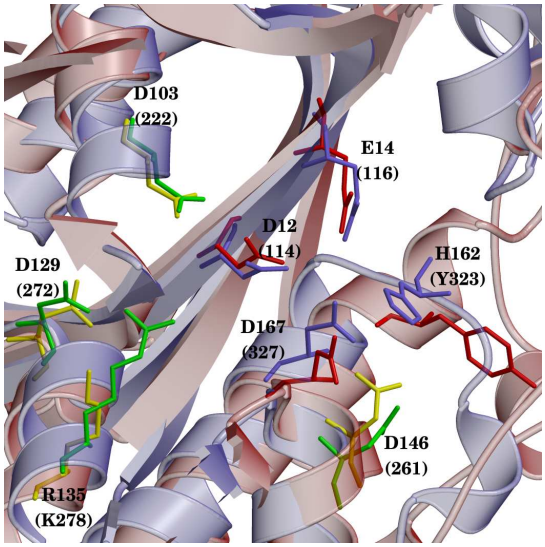

[1] Case D. A., T.E. Cheatham III, Darden T. A., Gohlke H., Luo R., K.M. Merz Jr., Onufirev A., Simmerling C., Wang B., & Woods R. J. (2005) The amber biomolecular simulation programs *J. Comp. Chem.* **26**, 1668–1688.

[2] Frisch M. J., Trucks G. W., Schlegel H. B., Scuseria G. E., Robb M. A., Cheeseman J. R., Montgomery J. A., Jr., Vreven T., Kudin K. N., Burant J. C., Millam J. M., Iyengar S. S., Tomasi J., Barone V., Mennucci B., Cossi M., Scalmani G., Rega N., Petersson G. A., Nakatsuji H., Hada M., Ehara M., Toyota K., Fukuda R., Hasegawa J., Ishida M., Nakajima T., Honda Y., Kitao O., Nakai H., Klene M., Li X., Knox J. E., Hratchian H. P., Cross J. B., Bakken V., Adamo C., Jaramillo J., Gomperts R., Stratmann R. E., Yazyev O., Austin A. J., Cammi R., Pomelli C., Ochterski J. W., Ayala P. Y., Morokuma K., Voth G. A., Salvador P., Dannenberg J. J., Zakrzewski V. G., Dapprich S., Daniels A. D.,

Strain M. C., Farkas O., Malick D. K., Rabuck A. D., Raghavachari K., Foresman J. B., Ortiz J. V., Cui Q., Baboul A. G., Clifford S., Cioslowski J., Stefanov B. B., Liu G., Liashenko A., Piskorz P., Komaromi I., Martin R. L., Fox D. J., Keith T., Al-Laham M. A., Peng C. Y., Nanayakkara A., Challacombe M., Gill P. M. W., Johnson B., Chen W., Wong M. W., Gonzalez C., , & Pople J. A. (2004) *Gaussian 03, Revision D.02.* (Gaussian, Inc., Wallingford, CT).

[3] Ponder J. (1998) *TINKER, Software Tools for Molecular Design, Version 3.6: the most updated version for the TINKER program can be obtained from J.W. Ponder's WWW site at http://dasher.wustl.edu/tinker.* (Washington University, St. Louis).

[4] Zhang Y., Liu H., & Yang W. (2000) Free energy calculation on enzyme reactions with an efficient iterative procedure to determine minimum energy paths on a combined ab initio qm/mm potential energy surface *J. Chem. Phys.* **112**, 3483–3491.

[5] Zhang Y., Liu H., & Yang W. (2002) *"Ab Initio QM/MM and Free Energy Calculations of Enzyme Reactions", in Computational Methods for Macromolecules–Challenges and Applications* eds. Schlick T. & H.H.Gan. (Springer Verlag, Heidelberg, Germany), pp. 332–354.

[6] Zhang Y., Lee T., & Yang W. (1999) A pseudo-bond approach to combining quantum mechanical and molecular mechanical methods *J. Chem. Phys.* **110**, 46–54.

[7] Zhang Y. (2005) Improved pseudobonds for combined ab initio quantum mechanical/ molecular mechanical (qm/mm) methods *J. Chem. Phys.* **122**, 024114.

[8] Kirby T. W., Harven S., DeRose E. F., Chalov S., Chikova A. K., Perrino F. W., Schaaper R. M., London R. E., & Pedersen L. C. (2006) Structure of the *e. coli* dna polymerase iii ϵ–hot proofreading complex *J. Biol. Chem.* **281**, 38466–38471.

[9] Jorgensen W., Chandrasekhar J., Madura J., Impey R., & Klein M. (1983) Comparison of simple potential functions for simulating liquid water *J. Chem. Phys.* **79**, 926.

[10] Darden T. A., York D., & Pedersen L. G. (1993) Particle mesh ewald: an nlog(n) method for ewald sums *J. Chem. Phys.* **98**, 10089–10092.

[11] Essmann U., Perera L., Berkowitz M., Darden T. A., Lee H., & Pedersen L. G. (1995) A smooth particle mesh ewald method *J. Chem. Phys.* **103**, 8577–8593.

[12] Sagui C., Pedersen L. G., & Darden T. A. (2004) Towards an accurate representation of electrostatics in classical force fields: Efficient implementation of multipolar interactions in biomolecular simulations *J. Chem. Phys.* **120**, 73–87.

[13] Hamdan S., Carr P. D., Brown S. E., Ollis D. L., & Dixon N. E. (2002) Structural basis for proofreading during replication of the *escherichia coli* chromosome *Structure* **10**, 535–546.

[14] Becke A. D. (1993) Density–functional thermochemistry. iii, the role of exact exchange *J. Chem. Phys.* **98**, 5648–5652.

[15] Lee C., Yang W., & Parr R. G. (1988) Development of the colle-salvetti correlation energy formula into a functional of the electron density *Phys. Rev. B* **37**, 785–788.

[16] Liu S., Perera L., & Pedersen L. G. (2007) Binuclear manganese(ii) complexes in biological systems *Mol. Phys.* **105**, 2893–2898.

[17] Siegbahn P. E. M. (2001) A quantum chemical study of the mechanism of manganese catalase *Theo. Chem. Acc.* **105**, 197–206.

[18] Ivanov I. & Klein M. L. (2005) Dynamical flexibility and proton transfer in the arginase active site probed by ab initio molecular dynamics *J. Am. Chem. Soc.* **127**, 4010–4020.

[19] Hay P. J. & Wadt W. R. (1985) Ab initio effective core potentials for molecular calculations. potentials for k to au including the outermost core orbitals *J. Chem. Phys.* **82**, 299–310.

[20] Nayak S. & Jena P. (1998) Anomalous magnetism in small mn clusters *Chem. Phys. Lett.* **289**, 473–479.

[21] Rao B. & Jena P. (2002) Giant magnetic moments in nitrogen–doped mn clusters and their relevance to ferromagnetism in mn–doped gan *Phys. Rev. Lett.* **89**, 185504.

[22] Liu X., Liu X., Yue J., Yin Y., & Sun Y. (2004) A new polynuclear structure of malato manganese (ii) complex *J. Mol. Struct. THEOCHEM* **671**, 87–92.

[23] Cobar E. A., Khaliullin R. Z., Bergman R. G., & Head-Gordon M. (2007) Theoretical study of the rhenium–alkane interaction in transition metal–alkane σ–complexes *Proc. Natl. Acad. Sci.* **104**, 6963–6968.

[24] Burger S. K. & Yang W. (2006) Quadratic string method for determining the minimum–energy path based on multiobjective optimization *J. Chem. Phys.* **124**, 054109.

[25] Jónsson H., Mills G., & Jacobsen K. (1998) *"Nudged Elastic Band Method", in Classical and quantum dynamics in condensed phase simulations* eds. B.J.Berne, G.Ciccotti, & D.F.Coker. (World Scientific, Singapore), pp. 387–404.

[26] Maragakis P., Stefan A., Brumer Y., Reichman D., & Kaxiras E. (2002) Adaptive nudged elastic band approach for transition state calculation *J. Chem. Phys.* **117**, 4651–4658.

[27] Ayala P. & Schlegel H. (1997) A combined method for determining reaction paths, minima and transition state geometries *J. Chem. Phys.* **107**, 375–384.

[28] Liu H., Lu Z., Cisneros G. A., & Yang W. (2004) Parallel iterative reaction path optimization in *ab initio* quantum mechanical/molecular mechanical modeling of enzyme reactions *J. Chem. Phys.* **121**, 697–706.

[29] Cisneros G. A., Liu H., Lu Z., & Yang W. (2005) Reaction path determination for quantum mechanical/molecular mechanical modeling of enzyme reactions by combining first order and second order "chain–of–replicas" methods *J. Chem. Phys.* **122**, 114502.

[30] Xie L., Liu H., & Yang W. (2004) Adapting the nudged elastic band method for determining minimum energy paths of chemical reactions in enzymes *J. Chem. Phys.* **120**, 8039–8052.

[31] Press W. H., Teukolsky S. A., Vetterling W. T., & Flannery B. P. (1992) *Numerical recipes in fortran77; the art of scientific computing, 2nd Ed.* (Cambridge University Press, New York, NY).

[32] Chu J.-W., Trout B. L., & Brooks B. R. (2003) A super–linear minimization scheme for the nudged elastic band method *J. Chem. Phys.* **119**, 12708–12716.

[33] Cisneros G. A., Wang M., Silinski P., Fitzgerald M., & Yang W. (2006) Theoretical and experimental determination on two substrates turned over by 4–oxalocrotonate tautomerase *J. Phys. Chem. A* **110**, 700–708.

[34] Gonzalez C. & Schlegel H. (1990) Reaction path following in mass–weighted internal coordinates *J. Phys. Chem.* **94**, 5523–5527.

[35] Schlegel H. (2003) Exploring potential energy surfaces for chemical reactions: an overview of some practical methods *J. Comp. Chem.* **24**, 1514–1527.

[36] Williams I. & Maggiora G. (1982) Use and abuse of the distinguished–coordinate method for transition state structure searching *J. Mol. Struct.* **89**, 365–378.

[37] Cisneros G. A., Liu H., Zhang Y., & Yang W. (2003) Ab–initio qm/mm study shows there is no general acid in the reaction catalyzed by 4–oxalocrotonate tautomerase *J. Am. Chem. Soc.* **125**, 10348–10393.

[38] Liu H., Zhang Y., & Yang W. (2000) How is the active–site of enolase organized to achieve overall efficiency in catalyzing a two step reaction *J. Am. Chem. Soc.* **122**, 6560–6570.

[39] Brautigam C. A., Sun S., Piccirilli J. A., & Steitz T. A. (1999) Structures of normal single–stranded dna and deoxyribo–3′–s–phosphothiolates bound to the 3′–5′ exonucleolytic active site of dna polymerase i from *escherichia coli Biochemistry* **38**, 696–704.

[40] Shamoo Y. & Steitz T. A. (1999) Building a replisome from interacting pieces: Sliding clamp complexed to a peptide from dna polymerase and polymerase editing complex *Cell* **99**, 155–166.

[41] Lee-Kirsch M. A., Gong M., Choudhury D., , Senenko L., Engel K., Lee Y.-A., deSilva U., Bailey S. L., Witte T., Vyse T. J., Kere J., Pfeiffer C., Harvey S., Wong A., Koskenmies S., Hummel O., Rhode K., Schmidt R. E., Dominiczak A. F., Gahr M., Hollis T., Perrino F. W., Lieberman J., & Hübner H. (2007) Mutations in the gene encoding the 3′–5′ dna exonuclease trex1 are associated with systemic lupus erythematosus *Nat. Gen.* **39**, 1065–1067.

[42] Rice G., Newman W. G., Dean J., Patrick T., Parmar R., Flintoff K., Robbins P., Harvey S., Hollis T., O'Hara A., Herrick A. L., Bowden A. P., Perrino F. W., Lindahl T., Barnes D. E., & Crow Y. J. (2007) Heterozygous mutations in trex1 cause familial chilblain lupus and dominant aicardi–goutières syndrome *Am. J. Hum. Gen.* **80**, 811–815.

[43] Lee-Kirsch M. A., Choudhury D., Harvey S., Gong M., Seneko L., Engel K., Pfeiffer C., Hollis T., Perrino F. W., Lieberman J., & Hübner H. (2007) A mutation in trex1 that impairs susceptibility to granzyme a–mediated cell death underlies familial chilblain lupus *J. Mol. Med.* **85**, 531–537.